# *In Situ* Fabrication of Silver Peroxide Hybrid Ultrathin Co-based MOFs for Enhanced Chemodynamic Antibacterial Therapy

Mengmeng Xu [a], Fangrong Tan [a], Wanru Luo [a], Yifan Jia [a], Yan Deng [a], Paul D. Topham [b], LinGe Wang [a, *] and Qianqian Yu [a, *]

[a] South China Advanced Institute for Soft Matter Science and Technology, School of Emergent Soft Matter, Guangdong Provincial Key Laboratory of Functional and Intelligent Hybrid Materials and Devices, South China University of Technology, Guangzhou 510640, P. R. China.

[b] Chemical Engineering and Applied Chemistry, School of Infrastructure and Sustainable Engineering, College of Engineering and Physical Sciences, Aston University, Birmingham, B47ET, UK.

**ABSTRACT:**

Bacterial-induced infectious diseases have always caused an unavoidable problem and lead to an increasing threat to human health. Hence, there is urgent need for effective anti-bacterial strategies to treat infectious diseases. Current methods are often ineffective and require large amounts of hydrogen peroxide ($H_2O_2$), with harmful effects on normal healthy tissue. Chemodynamic therapy (CDT) provides an ideal infection microenvironment (IME)-activated paradigm to tackle bacterial related diseases. To take full advantage of the specificity of IME and enhanced CDT for wounds with bacterial infection, we have designed an intelligent antibacterial system that exploits nanocatalytic ZIF-67@$Ag_2O_2$ nanosheets. In this system, silver peroxide

nanoparticles ($Ag_2O_2$ NPs) were grown on ultrathin zeolitic imidazolate framework-67 (ZIF-67) nanosheets by *in situ* oxidation and then ZIF-67@$Ag_2O_2$ nanosheets with the ability to self-generate $H_2O_2$ were triggered by the mildly acidic environment of IME. Lamellar ZIF-67 nanosheets were shown to rapidly degrade and release $Co^{2+}$, allowing conversion of less reactive $H_2O_2$ into the highly toxic reactive oxygen species (ROS) hydroxyl radicals (•OH), for enhanced CDT antibacterial properties. *In vivo* results revealed that the ZIF-67@$Ag_2O_2$ nanosheets system exhibits excellent antibacterial performance against both Gram-positive (*S. aureus*) and Gram-negative (*E. coli*) bacteria. The proposed hybrid strategy demonstrates a promising therapeutic strategy to enable antibacterial agents with IME-responsive nanocatalytic activity to circumvent antibiotic resistance against bacterial infections.

**KEYWORDS:** Chemodynamic therapy, Antibacterial effect, Wound healing, ZIF-67 nanosheets, IME-activated.

## 1 INTRODUCTION

Bacterial-induced wound disinfection is required to heal wounds that endanger human health.[1, 2] Antibiotics play an irreplaceable role in the clinical treatment to fight infections caused by bacteria.[3,4] However, abuse of antibiotics can lead to the formation of multidrug-resistant bacteria and biofilm formation.[5, 6] Thus, it is urgent to develop non-antibiotic antibacterial technologies and agents.[7] Recently, there have been advances in the development of ROS-mediated antibacterial strategies as an alternative

to traditional therapies.[8, 9] Chemodynamic therapy (CDT) is a promising antibacterial modality that is based on the *in situ* conversion of $H_2O_2$ into highly toxic •OH in the infection microenvironment (IME) via Fenton or Fenton-like reactions mediated by catalytic metal ions (e.g. $Co^{2+}$, $Fe^{2+}$, $Mn^{2+}$ *et al*).[10, 11] Despite the promise of CDT, its development for tools with effective bacterial killing has been limited. For example, although the IME has a high $H_2O_2$ level, endogenous $H_2O_2$ is still insufficient to generate adequate •OH for satisfactory CDT efficacy.[12] Moreover, the IME is also acidic (pH 5.5~7.0), and pH-responsive nanoplatforms are therefore recognized as an ideal candidate to operate in the target site and overcome the limitations of CDT.[13, 14, 15, 16] Therefore, there is a huge need for creative strategies to address these limitations for effective application.[17]

Recent efforts have been made to selectively increase the level of $H_2O_2$ in the IME.[18, 19] Among those, metal peroxide nanoparticles have been developed as an $H_2O_2$ self-sufficient material with good physicochemical characteristics and unique biological outcomes.[20, 21] Moreover, metal peroxide nanoparticles can act as solid-state precursors to self-provide $H_2O_2$ under acidic conditions without additional external stimulation. Subsequently, $H_2O_2$ is converted into •OH through a transition-metal Fenton-like reaction.[22] Several metal peroxide nanoparticles have been developed for biomedical applications. For example, Wang *et al*.[23] showed that zinc peroxide ($ZnO_2$) nanoparticles can delivers exogenous $H_2O_2$ and $Zn^{2+}$ with the capability of intensifying endogenous ROS production for synergistic cancer therapy. Zhang *et al*[24]. assembled PVDF/carbon sphere@$TiO_2$ (PVDF/CST) composite membranes and demonstrated

their dye scavenging and bacteria inactivation under visible light. Gao $et$ $al.$[25] showed

that CaO$_2$@DOX@ZIF-67 simultaneously supplies H$_2$O$_2$ and O$_2$ to achieve improved

chemo/chemodynamic therapy, and Li $et$ $al.$[26] synthesized pomegranate-like

CuO$_2$@SiO$_2$ nanospheres as O$_2$ and H$_2$O$_2$ generators for enhanced antibacterial activity.

For practical use in antibacterial applications, metal peroxide nanoparticles can provide

excellent H$_2$O$_2$ performance and the composed metal ions can help to counter

antibacterial infections.[27, 28, 29, 30, 31]

Metal-organic frameworks (MOFs) are emerging porous materials with large surface

area, metal-containing clusters and tunable structure, making them highly attractive as

powerful platforms for diverse applications.[32, 33, 34] Zeolitic imidazolate frameworks

(ZIFs) composed of transition metal cations and imidazolate ligands can exhibit Fenton

or Fenton-like reaction activity by introducing cobalt or other metallic elements as a

metal node.[12, 35] In particular, a cobalt-based zeolitic imidazolate framework (ZIF-67)

has been developed for antibacterial use owing to given the favorable biocompatibility

and acid degradation capacity of this material.[36, 37, 38, 39, 40] Recently, Chen et al.[41]

synthesized a series of ZIF-67 with different morphology and sizes, and demonstrated

that these nanostructures exhibited enhanced antibacterial activity against

saccharomyces cerevisiae. Importantly, the large surface area of ZIF nanosheet

materials facilitates the access of substrate molecules to surface active sites with smaller

diffusion barriers than those of bulk ZIFs.[42, 43] Thus, compared to conventional bulk

ZIFs, ZIF nanosheets offer better potential for biocatalytic applications.[44, 45]

The ideal nanoparticles not only deliver a strong CDT- mediated therapeutic effect to

the sites of infection, but also limit the effects to these sites while leaving healthy tissues unaffected. Therefore, the pursuit of these traits present a significant challenge in the development of antibacterial nanoparticles.[46, 47, 48]

Given this ultimate ambition, we have developed a degradable nanocatalytic ZIF-67 based antibacterial (ZIF-67@Ag$_2$O$_2$) platform. This system acts as a self-activated cascade reagent that not only releases Ag$^+$ and H$_2$O$_2$ from Ag$_2$O$_2$, but also releases Co$^{2+}$ that reacts with H$_2$O$_2$ to generate toxic •OH through Fenton-like reactions in the acidic bacterial IME for efficient antibacterial activity (Scheme 1). After demonstrating the biocompatibility of this nanocatalytic material, a skin infection model was adopted to test the bacterial elimination ability *in vivo*. The results show that the novel constructed nanocatalytic system could realize high-performance antibacterial effects and provide a promising CDT antibacterial strategy.



**Scheme 1.** Illustration of ZIF-67@Ag$_2$O$_2$ nanosheet synthesis route (A) and the *in vivo* antibacterial mechanism (B).

## 2. MATERIALS AND METHODS

### 2.1 MATERIALS

All chemicals were obtained from commercial suppliers and used without further purification, cobalt nitrate hexahydrate (Co(NO$_3$)$_2$·6H$_2$O), cetyltrimethylammonium bromide (CTAB), 2-Methylimidazole (2-mim), *N,N*-dimethylformamide (DMF), silver nitrate (AgNO$_3$, 99.8%), sodium hydroxide (NaOH, 96%), poly(vinylpyrrolidone) (PVP, M$_W$ = 1.0×10$^4$ g·mol$^{-1}$ ), hydrogen peroxide (H$_2$O$_2$, 30%), acetate anhydrous (NaAc, 99.0%), 3,3′,5,5′-tetramethylbenzidine (TMB, 99.0%), methylene blue (MB), 5,5-dimethyl-1-pyrroline *N*-oxide (DMPO) and acetic acid (HAc, 99.5%) were obtained from Aladdin Chemical Reagent Co., Ltd. (China). Luria-Bertani (LB) broth, Phosphate buffered saline (PBS) powder, and LB agar powder were purchased from Qingdao Hope Bio-Technology Co., Ltd. (China). Acridine orange/propidium iodide (AO/PI), high-glucose DMEM, fetal bovine serum (FBS; Gibco), 1% penicillin/streptomycin, 2',7'-dichlorodihydro fluorescein diacetate (DCFH-DA), 4% paraformaldehyde, cell counting kit-8 (CCK-8) assay, FITC-phalloidin were purchased from Beijing Solarbio Science & Technology Co., Ltd., China. Other reagents and solvents were of analytical grade and were used without any further purification, unless otherwise noted.

### 2.2 METHODS

**Synthesis of ZIF-67 nanosheets**

The ZIF-67 nanosheets were created using a previous protocol with a slight modification.[49] In a typical preparation process, an aqueous CTAB solution (70 mL, 4.3

mg·mL$^{-1}$) was magnetically stirred for 30 minutes at 30 °C, before a Co(NO$_3$)$_2$·6H$_2$O solution (375 μL, 0.5 mol·L$^{-1}$) was added, stirred again for 30 minutes, and dimethylimidazole solution (7.5 mL, 1.096 mol·L$^{-1}$) was added with a micro-syringe pump before further stirring for 1 hour. Finally, the solution was washed three times with DMF and methanol, to produce the ZIF-67 nanosheet sample.

**Synthesis of ZIF-67@Ag$_2$O$_2$ nanosheets**

The ZIF-67@Ag$_2$O$_2$ nanosheets were created following a previously reported protocol with a slight modification.[50] In this procedure, AgNO$_3$ (5 mL, 20 mmol·L$^{-1}$) was added to an aqueous solution that contained 100 mg of ZIF-67 nanosheets in a 1.0 mmol·L$^{-1}$ PVP solution. Then, H$_2$O$_2$ (150 mL, 30%) and NaOH (5 mL, 20 mmol·L$^{-1}$) were sequentially added to the solution. The PVP-coated ZIF-67@Ag$_2$O$_2$ nanosheets were collected by centrifugation and repeatedly rinsed with ultrapure water and ethanol after 30 minutes of stirring. The finished product was lyophilized using a freeze-drier and kept in the dark under an inert atmosphere for storage prior to use.

**Colorimetric method assay of peroxo groups**

Potassium permanganate (KMnO$_4$, 50 μg·mL$^{-1}$) was dissolved in an aqueous solution containing H$_2$SO$_4$ (0.1 mol·L$^{-1}$). The solution was treated with PBS (control), ZIF-67 nanosheets, Ag$_2$O$_2$ NPs, Ag$_2$O NPs, Ag NPs, H$_2$O$_2$ or ZIF-67@Ag$_2$O$_2$ nanosheets for 10 minutes. Subsequently, optical photographic images of the color change were taken, and the UV-vis spectra were collected.

**Detection of hydrogen peroxide (H$_2$O$_2$) and hydroxyl radical (·OH)**

Firstly, H$_2$O$_2$, Ag$_2$O$_2$ NPs, Ag$_2$O NPs or ZIF-67@Ag$_2$O$_2$ nanosheets were added to

separate 20 mL aliquots of PBS at pH 6.0 and stirred at 37 °C. The release of $H_2O_2$ was measured by the $H_2O_2$ detection kit and •OH concentration was monitored by specific TMB and MB probes. Briefly, the •OH release was investigated in 10 mM PBS at pH 6.0 with TMB (1.0 mM) was utilized as the molecular probe with a characteristic absorption peak at 652 nm for oxidized TMB. Control tests were carried out in 10 mM $H_2O_2$ and 1.0 mM TMB with ZIF-67 nanosheets, respectively. The degradation of MB was detected by mixed 10 $\mu g \cdot mL^{-1}$ MB, 10 mM $H_2O_2$, ZIF-67 nanosheets or ZIF-67@$Ag_2O_2$ nanosheets into buffer with at pH 6.0, and measured the optical absorption at 650 nm. The degradation of MB by •OH generated from ZIF-67@$Ag_2O_2$ nanosheets was further investigated with UV-vis absorbance spectra recording every 10 minutes for 180 minutes. Moreover, the presence of •OH was also confirmed by ESR spectroscopy at room temperature, using DMPO as the trapping agent of •OH.

**Cell culture and cell viability test**

HUVECs were used in this study. The cells were cultured in DMEM (high-glucose) supplemented with FBS (10%) and penicillin/streptomycin (1%) and cultured in a humidified incubator (5% $CO_2$, 37 °C). The cell viability of the HUVECs was assessed by CCK-8 assay. Different concentrations of ZIF-67@$Ag_2O_2$ nanosheets (5, 10, 20, 40, 60, 80 and 100 $\mu g \cdot mL^{-1}$) were co-incubated with cells for 24 hours. The absorbance of each well at 490 nm was recorded on a microplate reader and the cell viability was calculated.

Moreover, morphological observation of HUVEC cells were observed by confocal laser scanning microscopy (CLSM 880, Zeiss, Germany). In brief, after ZIF-

67@Ag$_2$O$_2$ nanosheets (50 μg·mL$^{-1}$) were co-incubated for 24 hours. HUVECs were immobilized with paraformaldehyde (4%) for 30 minutes. The cell cytoskeleton and nuclei were counterstained with DAPI for 5 minutes and FITC-phalloidin for 30 minutes, respectively. Finally, the samples were washed twice with PBS, and observed by CLSM.

**Hemolysis test**

A hemolysis test was used to confirm the blood compatibility of the ZIF-67@Ag$_2$O$_2$ nanosheets. Briefly, rat red blood cells (RBCs) were suspended in 10 mL PBS. Then, the ZIF-67@Ag$_2$O$_2$ nanosheets at different concentrations were added into the RBC suspensions (50 μL). Ultra-pure water served as a positive control; PBS buffer as a negative control, each were incubated for 2 hours at 37 °C, before these mixtures were centrifuged (8000 rpm, 5 minutes). Subsequently, the absorbance values at 450 nm were recorded. The hemolysis ratio was calculated as follows equations (1):

$$\text{Hemolysis rate (\%)} = (N - Na) / (Np - Na) \times 100\% \tag{1}$$

Where $N$, $Na$ and $Np$ represent the absorbance of RBC exposed to ZIF-67@Ag$_2$O$_2$ nanosheets, negative control, and positive control, respectively.

**Bacterial cultivation**

Luria−Bertani (LB) broth and LB agar were prepared according to the formula for bacterial culture. Escherichia coli (*E. coli*) and Staphylococcus aureus (*S. aureus*) were used as Gram-negative and Gram-positive bacterial strains for our antibacterial research. A mono-colony of *E. coli* or *S. aureus* formed in the solid (LB) medium was inoculated in liquid LB medium shaking with 100 rpm (37 °C, 12 hours).

### *In vitro* bacterial ROS detection

ROS level evaluation in bacteria was undertaken using a commercial modified oxidation sensitive fluorescent probe of DCFH-DA. After treatment, DCFH-DA in serum-free medium was incubated with bacteria for 30 minutes (37 °C), and then the cells were washed three times with PBS to remove unloaded DCFH-DA. To confirm the presence of ROS, samples were imaged by CLSM to observe green fluorescence.

### Live/dead staining test

After the various treatment protocols, the bacterial suspensions were stained with AO/PI. The samples were incubated for 10 minutes at 37 °C, followed by three washes with PBS. CLSM was used to observe dead (red) and live (green) bacteria.

### Morphological observation of the bacterial

After the different treatments, the morphological change of the bacteria was observed by scanning electron microscopy (SEM, JEOL JSM-7900F, Japan). To the polyformaldehyde of the fixed samples, all the samples were dehydrated by adding a series of ethanol solutions at different concentrations (10%, 30%, 50%, 70%, and 90%) for 10 minutes each time. Finally, the bacterial samples were freeze-dried and characterized by SEM after platinum sputter coating.

### Antibacterial assay

The antibacterial capability of ZIF-67@$Ag_2O_2$ nanosheets was assessed by the Standard plate counting method and antibacterial ratio. Typically, *S. aureus* and *E. coli* cell suspensions and $H_2O_2$ (100 μM), ZIF-67 nanosheets, $Ag_2O_2$ NPs and ZIF-67@$Ag_2O_2$ nanosheets (50 μg·mL$^{-1}$, pH 6.0 or 7.4) were mixed and incubated on a

shaking plate for 4 hours (100 rpm, 37 °C). 100 µL of the mixture was then removed, diluted by 10,000 in PBS, and coated in solid LB medium, before co-incubation for 12 hours (37 °C). Bacterial survival rate was calculated as follows equations (2):

$$\text{Bacterial survival rate (\%)} = CFU_{\text{(experiments group)}}/CFU_{\text{(control group)}} \times 100\% \tag{2}$$

**Establishment of the infectious skin wound model**

To evaluate the *in vivo* antibacterial property of ZIF-67@Ag$_2$O$_2$ nanosheets, an infectious skin wound model on the upper back of healthy female kun ming mice (AEC No. 2020048) was established. In this study, all animal study protocols were performed in compliance with the guidelines of the Institutional Animal Care and Use Committee of the Department of the South China University of Technology. Infectious skin wounds were excised by nicking each mouse with a sterile scalpel (approximately 6 × 6 mm). Then *S. aureus* (1.0 × 10$^9$ CFU, 100 µL) was inoculated onto the back of mice to construct an infected wound model. After 48 hours, the mice were randomly divided into five groups (n=3), and the infected mice were treated with PBS, H$_2$O$_2$ (100 µM), ZIF-67 nanosheets, Ag$_2$O$_2$ NPs or ZIF-67@Ag$_2$O$_2$ nanosheets (50 µg·mL$^{-1}$). After the relevant treatment, in all groups, the body weight of the mouse was recorded and the wound sizes of the mice were measured perpendicularly ($d_1 < d_2$). The wound area S and relative wound area rate (%) was calculated as follows equations (3 and 4):

$$S = \pi d_1 \times d_2 / 4 \tag{3}$$

$$\text{Relative wound area(\%)} = A_i / A_o \times 100\% \tag{4}$$

where $A_o$ is the initial wound area and $A_i$ is the wound area following treatment.

At 15 days, the wound skin samples were dissected for histopathological

hematoxylin and eosin (H&E) staining, immunohistochemistry staining (CD31) and Masson's trichrome staining analysis. Furthermore, the main organs (heart, liver, spleen, lung, and kidney) were collected for H&E staining and measured by Wuhan Servicebio technology Co., Ltd (China). Meanwhile, the wound was excised for high-speed homogenization. The tissue homogenate was diluted 10,000 times, and coated in solid LB medium, cultured at $37^{\circ}$C for 12 hours and viable colonies were imaged by digital camera.

**Enzyme-linked immunosorbent assay (ELISA) analysis**

Blood samples were collected from each mouse in each group on the 14th day, and then ELISA was performed to quantitatively measure the protein expression levels of TNF-α, interleukin (IL)-1β and IL-6 according to the instructions (ELISA, Beyotime Biotechnology).

## 3. RESULTS AND DISCUSSION

### 3.1 Synthesis and characterizations of ZIF-67@Ag$_2$O$_2$ nanosheets

Multi-functional synergistic antibacterial ZIF-67@Ag$_2$O$_2$ nanosheets were initially synthesized as described in a previous report with the following described changes, as shown in Scheme 1.[49, 50] The two-dimensional morphologies of ZIF-67 nanosheets and ZIF-67@Ag$_2$O$_2$ nanosheets were first observed by transmission electron microscopy (TEM) and SEM. The images in Figure 1A and 1B reveal the hexagonal sheet-like structure of the ZIF-67 nanosheets. Meanwhile, the atomic force microscopy (AFM) images (Figure S1A and S1B) show ZIF-67 nanosheets with average thickness of

approximately 17.4 nm and an average diameter of around $200 \pm 18.3$ nm, consistent with the TEM and SEM results. X-ray powder diffraction (XRD) experiments were performed to confirm the crystal structures of the ZIF-67 nanosheets. The observed sharp and strong characteristic peaks indicate the high degree of crystallinity of the ZIF-67 materials, consistent with the XRD patterns (Figure S2). To further confirm the successful preparation of ZIF-67 nanosheets, the samples were characterized by thermogravimetric analysis (TGA) from room temperature to 600 °C with a heating rate of 5 °C min$^{-1}$ in air atmosphere, as shown in Figure S3, The mass reduction at 100 °C is attributed to moisture loss prior to the degradation of the ZIF-67 nanosheets between 200 and 300 °C, consistent with previously reported data.[49]

The ZIF-67@Ag$_2$O$_2$ hybrid nanocatalyst was synthesized through the *in-situ* growth of Ag$_2$O$_2$ NPs *in situ* grown on a ZIF-67 nanosheet. TEM reveals that the sheet-like structure remained is preserved in the ZIF-67@Ag$_2$O$_2$ nanosheets (Figure 1C and Figure S4). The morphology of the Ag$_2$O$_2$ NPs can also be observed, indicating the successful modification of Ag$_2$O$_2$ NPs onto the surface of the ZIF-67 nanosheets. For precise elemental analysis of the nanosheet, elemental mapping was performed by energy dispersive spectroscopy (EDS). As shown in Figure 1D and Figure S5, the EDS elemental mapping reveals the uniform distribution of Ag and Co on the ZIF-67 nanosheets, and the homogeneous distribution of Co alone in the ZIF-67 nanosheet (Figure S6). Thus, the results directly confirm the successful fabrication of ZIF-67@ Ag$_2$O$_2$ nano-assemblies.

X-ray photoelectron spectroscopy (XPS) measurements were used to study the

elemental constitutions and the valence states of the ZIF-67@Ag$_2$O$_2$ nanosheets. As depicted in Figure 1E, the survey spectra of ZIF-67@Ag$_2$O$_2$ nanosheets demonstrate the presence of Co, Ag and O, with binding energy peaks at 530.71 eV, 531.49 eV and 532.78 eV that are assigned to C-O, Ag-O and O-O, respectively, suggesting that the existence of peroxo groups in ZIF-67@Ag$_2$O$_2$ nanosheets (Figure 1F). Of note, the Co 2p XPS spectrum (Figure S7A) displays two peaks (Co 2p$_{1/2}$ and Co 2p$_{3/2}$) at binding energies of 797.5 and 780.5 eV, respectively, suggesting the presence of Co (II) in ZIF-67@Ag$_2$O$_2$ nanosheets. For the Ag 3d XPS spectrum (Figure S7B)，there are two independent Ag 3d$_{3/2}$ and Ag 3d$_{5/2}$ peaks at the binding energies of 374.1 and 368.1 eV, respectively, indicating that the valence state of silver element is Ag (I). Furthermore, the presence of the peroxo groups in the ZIF-67@Ag$_2$O$_2$ nanosheets was confirmed by a KMnO$_4$-based colorimetric assay. As seen in Figure 1G, after addition of the acid-treated ZIF-67@Ag$_2$O$_2$ nanosheets, the color of MnO$_4^-$ solution turned from purple to colorless due to peroxo group-mediated reduction of MnO$_4^-$ to colorless Mn$^{2+}$. In contrast, the other groups (*i.e.* ZIF-67 nanosheets, Ag NPs, and Ag$_2$O NPs) did not induce a color change. This strongly indicates that Ag$_2$O$_2$ NPs and ZIF-67@Ag$_2$O$_2$ nanosheets produce H$_2$O$_2$ in acidic conditions. Decreased zeta potential values of the ZIF-67 nanosheets, Ag$_2$O$_2$ NPs, and ZIF-67@Ag$_2$O$_2$ nanosheets were also found. As shown in Figure S8, the zeta potential statistics show a clear change for ZIF-67 nanosheets from $22.7 \pm 0.1$ to $-14.6 \pm 1.45$ mV due to the loading of negatively charged Ag$_2$O$_2$ NPs, further confirming the successful synthesis of the ZIF-67@Ag$_2$O$_2$ nanosheets.
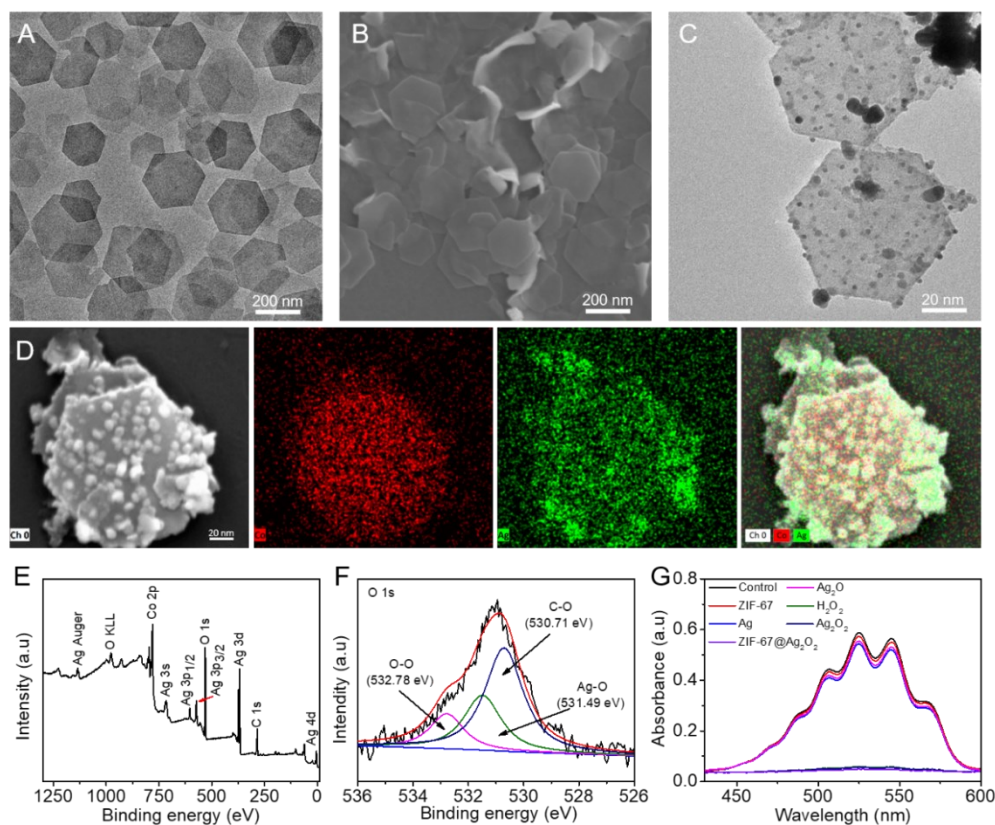
**Figure 1.** (A) TEM and SEM images (B) of sheet ZIF-67 nanosheets. (C) TEM images of ZIF-67@Ag$_2$O$_2$ nanosheets. (D) HAADF-STEM images and elemental mapping of ZIF-67@Ag$_2$O$_2$ nanosheets. (E) XPS survey spectra of ZIF-67@Ag$_2$O$_2$ nanosheets. (F) XPS spectra of O 1s in ZIF-67@Ag$_2$O$_2$ nanosheets. (G) Colorimetric analysis demonstrating the presence of peroxo groups under acidic conditions.

## 3.2 Detection of H$_2$O$_2$ and •OH

To investigate the pH-response of the ZIF-67@Ag$_2$O$_2$ nanosheets (Figure 2A), Co$^{2+}$ and Ag$^+$ release into PBS buffer solution was monitored by inductively coupled plasma optical emission spectroscopy (ICP-OES). As shown in Figure 2B and S9, accelerated Co$^{2+}$ and Ag$^+$ release from ZIF-67@Ag$_2$O$_2$ nanosheets occurred under mildly acidic conditions (pH 6.0), suggesting acid-triggered decomposition of ZIF-67@Ag$_2$O$_2$

nanosheets into $Co^{2+}$, $Ag^+$ and peroxo groups. In contrast, under neutral conditions (pH 7.4), ZIF-67@$Ag_2O_2$ nanosheets were stable with a relatively low level of $Co^{2+}$ and $Ag^+$ release.

To further verify this, we measured the morphology changed of ZIF-67@$Ag_2O_2$ nanosheets by TEM under different conditions. As shown in Figure S10, after dispersion at pH 7.4, the morphology of the ZIF-67@$Ag_2O_2$ nanosheets was unchanged for 2 hours, indicating the good stability of the ZIF-67@$Ag_2O_2$ nanosheets. Notably, at pH 6.0, ZIF-67@$Ag_2O_2$ nanosheets would be dissociated almost completely at 2 h, without significant solid nanoparticles present, indicating that both ZIF-67 and $Ag_2O_2$ were decomposed in the acidic condition. Subsequently, the $H_2O_2$ production capability of ZIF-67@$Ag_2O_2$ nanosheets was investigated by an $H_2O_2$ detection kit. As shown in Figure 2C, there was a distinct absorption signal at 430 nm, demonstrating the generation of $H_2O_2$ by the marked pH-responsive behavior of ZIF-67@$Ag_2O_2$ nanosheets.

To verify the Fenton-like reaction of ZIF-67@$Ag_2O_2$ nanosheets via the release of $Co^{2+}$, TMB was used as a capture probe that can be oxidized by •OH radicals to form oxTMB with a characteristic UV-vis absorption signal at 652 nm. As shown in Figures 2D and 2E, there was a distinct absorption signal in the presence of ZIF-67@$Ag_2O_2$ nanosheets and TMB, indicating that the ZIF-67@$Ag_2O_2$ nanosheets have $H_2O_2$ self-production capability due to the generation of •OH by Fenton-like activity under mildly acidic conditions (pH 6.0). To more quantitatively verify the production of •OH, ESR spectroscopy was performed using DMPO as an •OH trapping agent. As shown in

Figure 2F, there was no ESR signal from •OH in the control group. In contrast, a typical •OH signal (1:2:2:1) was detected in the ZIF-67@Ag$_2$O$_2$ nanosheets group, confirming the activated Fenton-like activity of ZIF-67@Ag$_2$O$_2$ nanosheets under mildly acidic conditions. The ability of ZIF-67@Ag$_2$O$_2$ nanosheets to generate •OH was also detected using MB degradation, as evidenced by a decrease in the absorption peak at 660 nm in the UV-vis spectra. As shown in Figures 2G and 2H, H$_2$O$_2$ alone cannot degrade MB, but MB can be degraded quickly when in the presence of H$_2$O$_2$ with either the ZIF-67 nanosheets or ZIF-67@Ag$_2$O$_2$ nanosheets (pH 6.0). As shown in Figure 2I, after reaction of ZIF-67@Ag$_2$O$_2$ nanosheets under mildly acidic conditions for 180 minutes, MB had almost completely degraded. The results indicate that reaction rates were under mildly acidic conditions with sustained release of •OH. This property would ensure the high efficiency of the ZIF-67@Ag$_2$O$_2$ nanosheets in antibacterial therapy under the typical physiological conditions of IME.
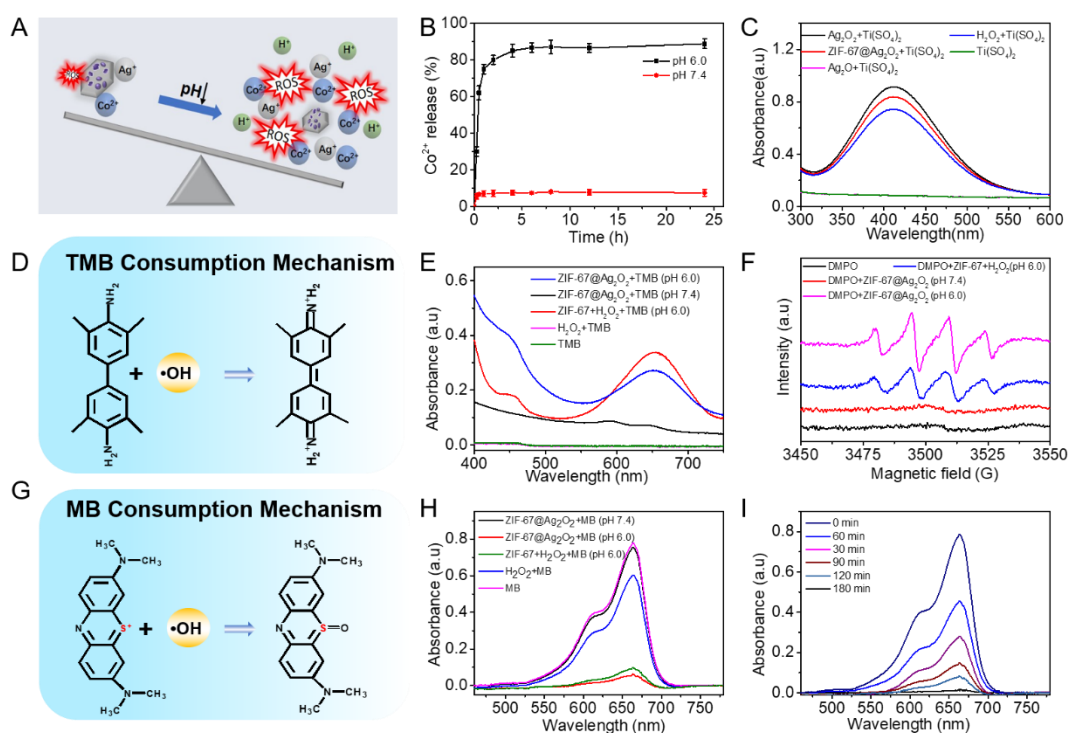
**Figure 2.** (A) Schematic illustration of •OH generation of ZIF-67@Ag$_2$O$_2$ nanosheets through cascade reactions under mildly acidic conditions. (B) Cumulative Co$^{2+}$ release from ZIF-67@Ag$_2$O$_2$ nanosheets at pH 6.0 and 7.4. (C) UV-vis spectra of the titanium peroxide complex in the presence of ZIF-67@Ag$_2$O$_2$ nanosheets or H$_2$O$_2$ (determined by H$_2$O$_2$ assay kit). (D) Mechanism of TMB consumption with •OH. (E) UV-vis absorbance of TMB after incubation with each formulation under mildly acidic conditions (pH 6.0). (F) ESR spectra of •OH from the mixture of formulation components captured by DMPO at acidic conditions. (G) Mechanism of MB consumption with •OH. (H) UV-vis spectra of various samples incubated with TMB under mildly acidic conditions. (I) UV-vis absorption spectra of the degradation process of MB solutions after treating with ZIF-67@Ag$_2$O$_2$ nanosheets under mildly acidic conditions (pH 6.0) at different time points. The data are shown as a mean ± SD (n = 3).

### 3.3. *In vitro* bacterial killing

As a kind of reactive oxygen species, •OH was highly oxidative and hence maintains the bactericidal effect. Encouraged by the superior properties of ZIF-67@Ag$_2$O$_2$ nanosheets to generate •OH, we carried out the following study to investigated their antibacterial properties *in vitro*. The standard plate counting method was applied to preliminarily assess the *in vitro* activity of this nanocatalyst against *E. coli* and *S. aureus* as target bacterial models. Viable concentrations of ZIF-67@Ag$_2$O$_2$ nanosheets ranging from 0 to 60 μg·mL$^{-1}$ were tested in the bacterial growth experiments. As shown in

Figures 3A to 3D, at a concentration of ZIF-67@Ag$_2$O$_2$ nanosheets of 60 μg·mL$^{-1}$ at

pH 6.0, there were few colonies on the plates, indicating the successful inactivation of

the majority of the bacteria and showed a concentration-dependent relationship.

Moreover, the synergistic antibacterial activity of ZIF-67@Ag$_2$O$_2$ nanosheets was

further explored with different treatment at both pH 6.0 and 7.4. For comparison and

simulation of wound IME, several groups were included: control (PBS), H$_2$O$_2$, ZIF-67

nanosheets, Ag$_2$O$_2$ NPs and ZIF-67@Ag$_2$O$_2$ nanosheets. As demonstrated in Figure 3E

to 3G, compared with the control group treated with PBS (1×10$^9$ CFU mL$^{-1}$), a certain

number of the *E. coli* or *S. aureus* bacterial colonies were observed after treatment with

H$_2$O$_2$, ZIF-67 nanosheets and Ag$_2$O$_2$ NPs alone at pH 7.4 and 6.0. Remarkably, for the

ZIF-67@Ag$_2$O$_2$ nanosheets at pH 6.0, almost no bacterial colonies were observed. This

dramatically enhanced antibacterial performance over other groups revealed that ZIF-

67@Ag$_2$O$_2$ nanosheets exhibit a superior elimination effect on *E. coli* and *S. aureus*

bacteria. What's more, to further understand the effect of the ratio of ZIF-67 to Ag$_2$O$_2$

on the antibacterial infection performance, incubation of *S. aureus* and *E. coli* with

different ZIF-67:Ag$_2$O$_2$ weight ratios was undertaken. As seen in Figure S11, the death

rates of *E. coli* and *S. aureus* were found to be 98.99% and 95.47%, respectively, at a

weight ratio of 1:1 ZIF-67:Ag$_2$O$_2$, suggesting that the high antibacterial activity of ZIF-

67@Ag$_2$O$_2$ was largely attributed to the synergistic antibacterial mechanism of ZIF-67

and Ag$_2$O$_2$. These results clearly suggest that ZIF-67@Ag$_2$O$_2$ composite nanosheets

display superior antibacterial efficiency than that of the pristine materials, which is

ascribed to an improved synergistic effect between the two materials.
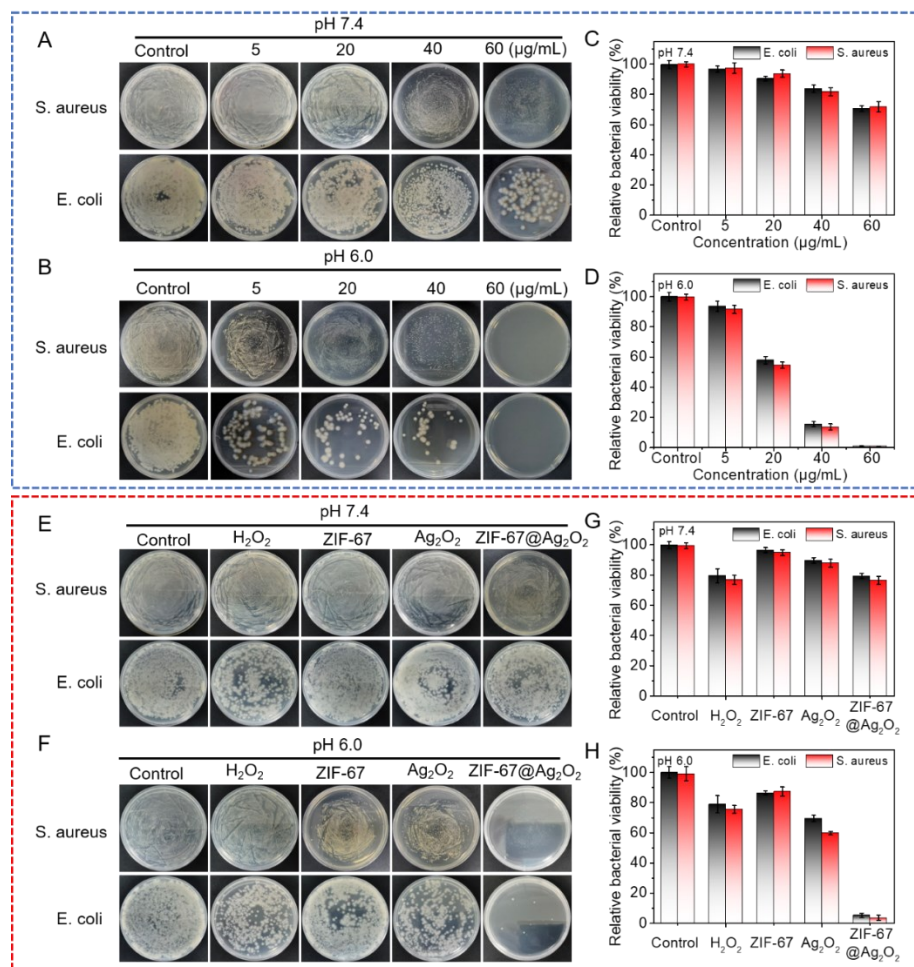
**Figure 3.** (A-B) Photographic images of bacterial colonies after treatment with ZIF-67@Ag$_2$O$_2$ nanosheets at different concentrations and pH (7.4 and 6.0). (C-D) Relative bacterial survival after being treated with ZIF-67@Ag$_2$O$_2$ nanosheets at different concentrations and pH (7.4 and 6.0). (E-F) Photographic images of bacterial colonies after treatment with different samples at the same concentration (50 μg·mL$^{-1}$) and at different pH (7.4 and 6.0). (G-H) Relative bacterial survival after various sample therapies at different pH (7.4 and 6.0). The data are shown as a mean ± SD (n = 3)

To further evaluate the antibacterial performance of the ZIF-67@Ag$_2$O$_2$ nanosheets,

the bacterial morphological changes of *S. aureus* and *E. coli* were evaluated by SEM after the various different treatments. As shown the SEM images (Figure 4A) of *S. aureus* and *E. coli* treated with PBS (group one) showed smooth, intact cell membranes. The cells of *E. coli* exhibited the typical rhabdoid shape and the *S. aureus* cells had smooth membranes with spherical structures. In the groups of $H_2O_2$, ZIF-67 nanosheets, $Ag_2O_2$ NPs and ZIF-67@$Ag_2O_2$ nanosheets at pH 7.4, there were few disruptions on the bacterial cell surface. This indicated normal growth of *S. aureus* and *E. coli* in the presence of these materials. In contrast, for the treatments at pH 6.0, the bacterial surface became partially wrinkled and disrupted, indicating weak antibacterial activity. In the ZIF-67@$Ag_2O_2$ nanosheets (pH 6.0) group, there were obvious cell wall fragments, deformation, and irregularly shaped holes on the cell surface, indicating severe bacterial damage. These are solid evidence suggest that the cell membrane of the bacteria was destroyed by toxic •OH generated from a cascade reaction, catalyzed by the ZIF-67@$Ag_2O_2$ nanosheets. Once there are holes in the cell membrane, the bacteria contents can leak out, leading to bacterial death. Similar results were also observed by alamar blue-staining. As shown in Figure 4B, there was significant color change to dark purple for the ZIF-67@$Ag_2O_2$ nanosheets group at pH 6.0, which indicates the bacterial most significant suppression. The antibacterial efficiency is shown in Figure 4C and is consistent with the above standard plate counting experimental results.

In addition to the SEM imaging and standard plate counting method, the synergistic antibacterial properties were directly investigated by live/dead staining using AO and

PI as the probes of live and dead bacteria, respectively. The results are shown in Figure 4D. *S. aureus* or *E. coli* treated with PBS, the ZIF-67 nanosheets or $Ag_2O_2$ NPs alone at pH 7.4 display green fluorescence. In contrast, red fluorescence visibly increased for ZIF-67 nanosheets and $Ag_2O_2$ NPs at pH 6.0, suggesting that the mildly acidic conditions induce some antibacterial activity. Notably, ZIF-67@$Ag_2O_2$ nanosheets presented almost completely red fluorescence in the mildly acidic environment, indicating excellent pH-responsive antibacterial activity of this material against *S. aureus and E. coli* bacteria. Taken together, all of the described results demonstrate that ZIF-67@$Ag_2O_2$ nanosheets can achieve satisfactory efficiency against both Gram-negative and Gram-positive bacteria by releasing highly active •OH for CDT.
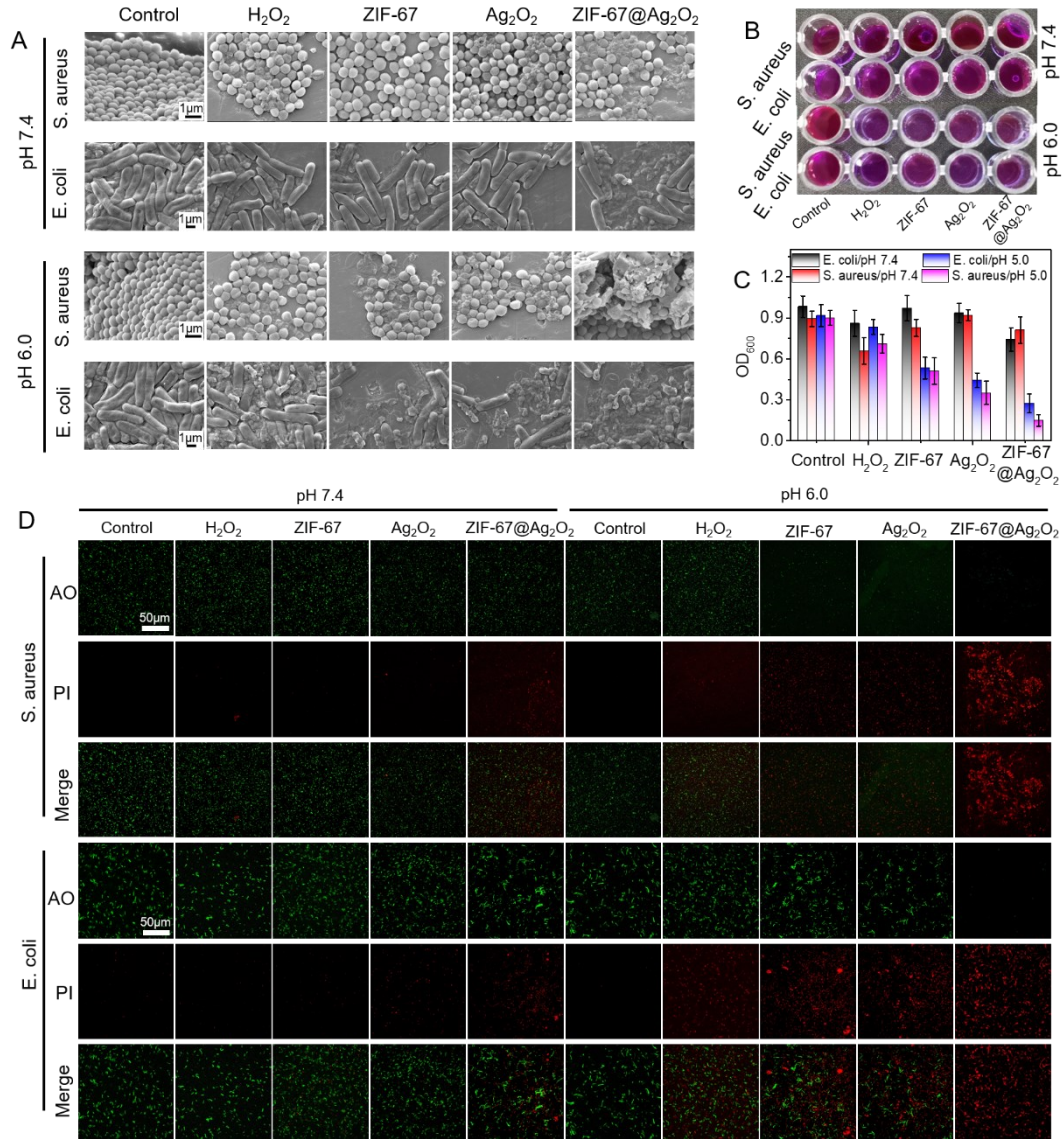
**Figure 4.** (A) SEM images of *E. coli and S. aureus* following treatment with each combination of the formulation components, at pH 7.4 or 6.0. (B) Photographs of alamar blue-staining at various treatments with pH 7.4 or 6. 0. (C) The $OD_{600}$ of *E. coli and S. aureus* treated with each combination of formulation components with pH 7.4 or 6.0. (D) Fluorescence images of *E. coli and S. aureus* with AO/PI dual florescence staining under various treatments. The data are shown as a mean ± SD (n = 3).

## 3.4 Antibacterial mechanism and biofilms treatment

Based on the above results, we hypothesize that the antibacterial effect of ZIF-67@Ag$_2$O$_2$ nanosheets was due to oxidative injury caused by the ROS storm (Figure 5A). To further investigate the antibacterial mechanism of the ZIF-67@Ag$_2$O$_2$ nanosheets, intracellular ROS levels were investigated using DCFH-DA as a ROS probe. DCFH-DA can be oxidized by ROS into 2' 7'-dichlorofluorescin (DCF), which exhibits green fluorescence (Figure 5B). In the control group, there was little detected green fluorescence after the various treatments, indicating there was virtually no ROS production at pH 7.4 or 6.0. A weak green fluorescence was observed for the H$_2$O$_2$ group and the Ag$_2$O$_2$ NPs group, indicating some generation of ROS. Distinctly, bright green fluorescence was observed in bacterial cells treated with ZIF-67@Ag$_2$O$_2$ nanosheets at pH 6.0, confirming the increased production of ROS as the basis for antibacterial activity.

Biofilms can serve as physical barriers to restrict the penetration of antibacterial agents, limiting effective control. Based on the excellent broad-spectrum antibacterial property of ZIF-67@Ag$_2$O$_2$ nanosheets, we continued to study the ability of ZIF-67@Ag$_2$O$_2$ nanosheets to disrupt biofilms by live/dead staining and observation by 3D CLSM. *E. coli* and *S. aureus* biofilms were cultured in glass dishes for 2 days. ZIF-67@Ag$_2$O$_2$ nanosheets were then added into the wells at pH 7.4 or 6.0. After 6 h of co-incubation, AO/PI staining was performed. As shown in Figure 5C, compared with H$_2$O$_2$, ZIF-67 nanosheets, and Ag$_2$O$_2$ NPs groups, treatment of both *E. coli* and *S. aureus* biofilms with ZIF-67@Ag$_2$O$_2$ nanosheets at pH 6.0 resulted in significant red fluorescence, indicating significant bacterial death due to the synergistic antibacterial

action of this material NPs.
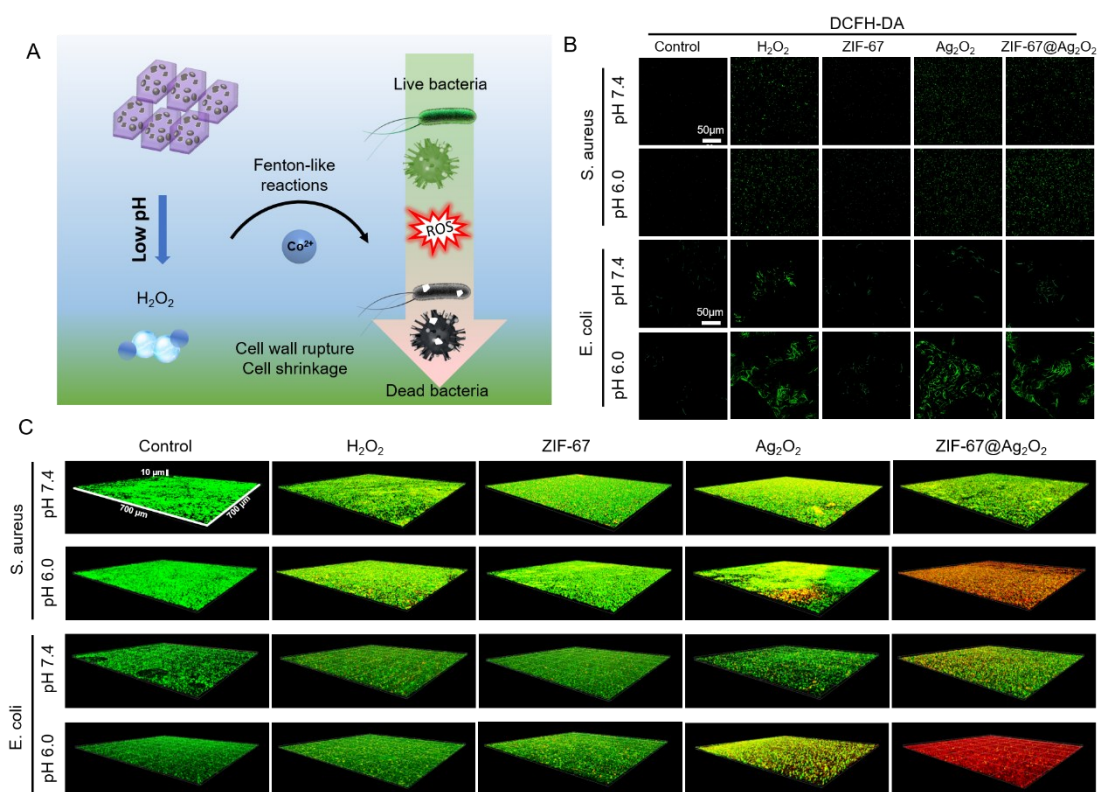


**Figure 5.** (A) Schematic of the disinfection mechanism of the ZIF-67@Ag$_2$O$_2$ nanosheets towards *S. aureus* and *E. coli*. (B) CLSM images of intracellular ROS production with the existence of DCFH-DA in *E. coli* and *S. aureus* incubated with different treatment (at pH 7.4 or 6.0) for 4 h. (C) 3D CLSM images of residual biofilms treated with each system at pH 7.4 or 6.0.

## 3.5 Cytotoxicity assay

Biosafety is an important prerequisite for the use of nanoparticles *in vivo*. Therefore, before performing animal experiments, we first investigated the cytotoxicity of ZIF-67@Ag$_2$O$_2$ nanosheets using HUVEC by CCK-8 assay. As shown in Figure 6A, the ZIF-67@Ag$_2$O$_2$ nanosheets showed no obvious cytotoxicity toward HUVECs even at 100 μg·mL$^{-1}$. The biosafety of ZIF-67@Ag$_2$O$_2$ nanosheets was next tested by a

hemolysis assay (Figure 6B). The hemolysis rate at the maximum experimental concentration (100 µg·mL$^{-1}$) was approximately 8.2 %, when ZIF-67@Ag$_2$O$_2$ nanosheets were cocultured with RBCs. Result shown a negligible degree of hemolysis caused by the ZIF-67@Ag$_2$O$_2$ nanosheets. The fluorescence image experiments further reveal the excellent biocompatibility of ZIF-67@Ag$_2$O$_2$ nanosheets as the cells maintained their cellular morphology intact (Figure 6C). These exciting findings demonstrate the good compatibility and lack of toxicity of ZIF-67@Ag$_2$O$_2$ nanosheets, making these materials appropriate for antibacterial treatment *in vivo*.
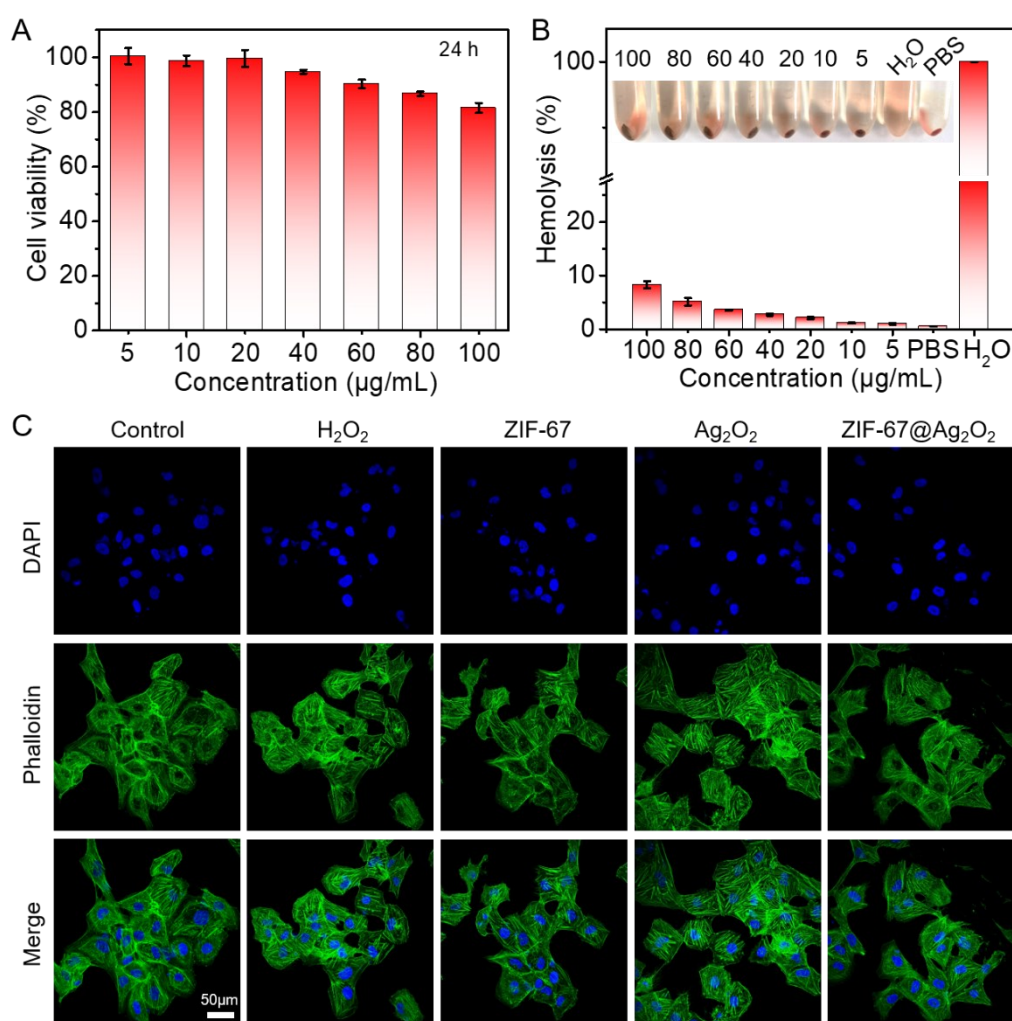


**Figure 6.** (A) Cell viability with various concentrations of ZIF-67@Ag$_2$O$_2$ nanosheets.

26

(B) Hemolysis percentage of RBCs at various concentrations of ZIF-67@Ag$_2$O$_2$ nanosheets. (C) Morphologies of cells cultured with ZIF-67@Ag$_2$O$_2$ nanosheets (50 μg·mL$^{-1}$) at different concentrations captured by CLSM (green: Phalloidin; blue: DAPI). The data are shown as a mean ± SD (n = 3).


## 3.6. *In vivo* wound healing and antibacterial performance

Encouraged by the excellent antibacterial ability and biocompatibility observed *in vitro*, we next analysed the antibacterial effect *in vivo* with an *S. aureus*-infected mouse skin wound model on the dorsal sites of mice. When bacteria infect a wound, a mildly acidic local environment is generated by the inflammatory cells in IME, which, based on our findings described herein, should be able to trigger the catalytic activity of ZIF-67@Ag$_2$O$_2$ nanosheets for antibacterial and wound healing behavior. The surgical procedures are shown in Figure 7A. Successfully infected mice were randomly assigned into five groups consisting of control (PBS), H$_2$O$_2$, ZIF-67 nanosheets, Ag$_2$O$_2$ NPs, and ZIF-67@Ag$_2$O$_2$ nanosheets. To observe the wound infection and healing process in each group, the mice wound sites were photographed every other day using a digital camera. As shown in Figures 7B and 7F, the photographic images indicate that rubbing H$_2$O$_2$ solution into a wound did not prevent the bacteria from interfering with wound healing and did not increase healing relative to the PBS group. Similar results were also observed for the ZIF-67 nanosheets and Ag$_2$O$_2$ NPs groups. However, ZIF-67@Ag$_2$O$_2$ nanosheets exhibited outstanding antibacterial activity and enhanced the wound closure process, with the wounds almost completely healed after 14 days of treatment. The

measurement of wound area rate (Figure 7C) reveals a faster healing effect when using the ZIF-67@Ag$_2$O$_2$ nanosheets. Thus, there is enhanced catalytic bacterial disinfection induced by •OH in wounds.

To further evaluate the antibacterial activity *in vivo* of different nanocomposites, Giemsa staining and H&E staining were conducted on days 2, and 4 after treatment of infected wound site. According to the H&E staining results (Figure S12), the samples used for the control group and different nanocomposite groups showed necrolysis of parenchymal cells, infiltration of lymphocytes and neutrophils, which represented severe inflammation and bacterial infection of the skin in the early stages of 2 day after treatment. Although neutrophils decreased by day 4, the H$_2$O$_2$, ZIF-67 nanosheets or Ag$_2$O$_2$ NPs groups still had some inflammatory cells. Notably, in the ZIF-67@Ag$_2$O$_2$ nanosheets group, there were significant decrease of inflammatory cells by day 4, demonstrating that ZIF-67@Ag$_2$O$_2$ has a significant antibacterial effect. This result was also confirmed by Giemsa staining. Compared to ZIF-67@Ag$_2$O$_2$ nanosheets groups, a large number of bacteria existed at the wound site of control, H$_2$O$_2$, ZIF-67 nanosheets or Ag$_2$O$_2$ NPs nanosheets groups on day 2, proving that the wound site had been successfully infected and lower antibacterial effect. When the wound was treated for 4 days, there were still a number of bacteria in the control group and the H$_2$O$_2$, ZIF-67 nanosheets or Ag$_2$O$_2$ NPs groups, while only very small amounts of bacteria were observed in the ZIF-67@Ag$_2$O$_2$ nanosheets groups after 4 days following treatment (Figure S13). This was consistent with the results of *in vitro* cell experiments where *S. aureus* cells from infected wound tissues were cultured and counted. As shown in

Figure 7E, the ZIF-67@Ag$_2$O$_2$ nanosheets had fewer bacterial colonies than all other groups after 14 days of treatment.
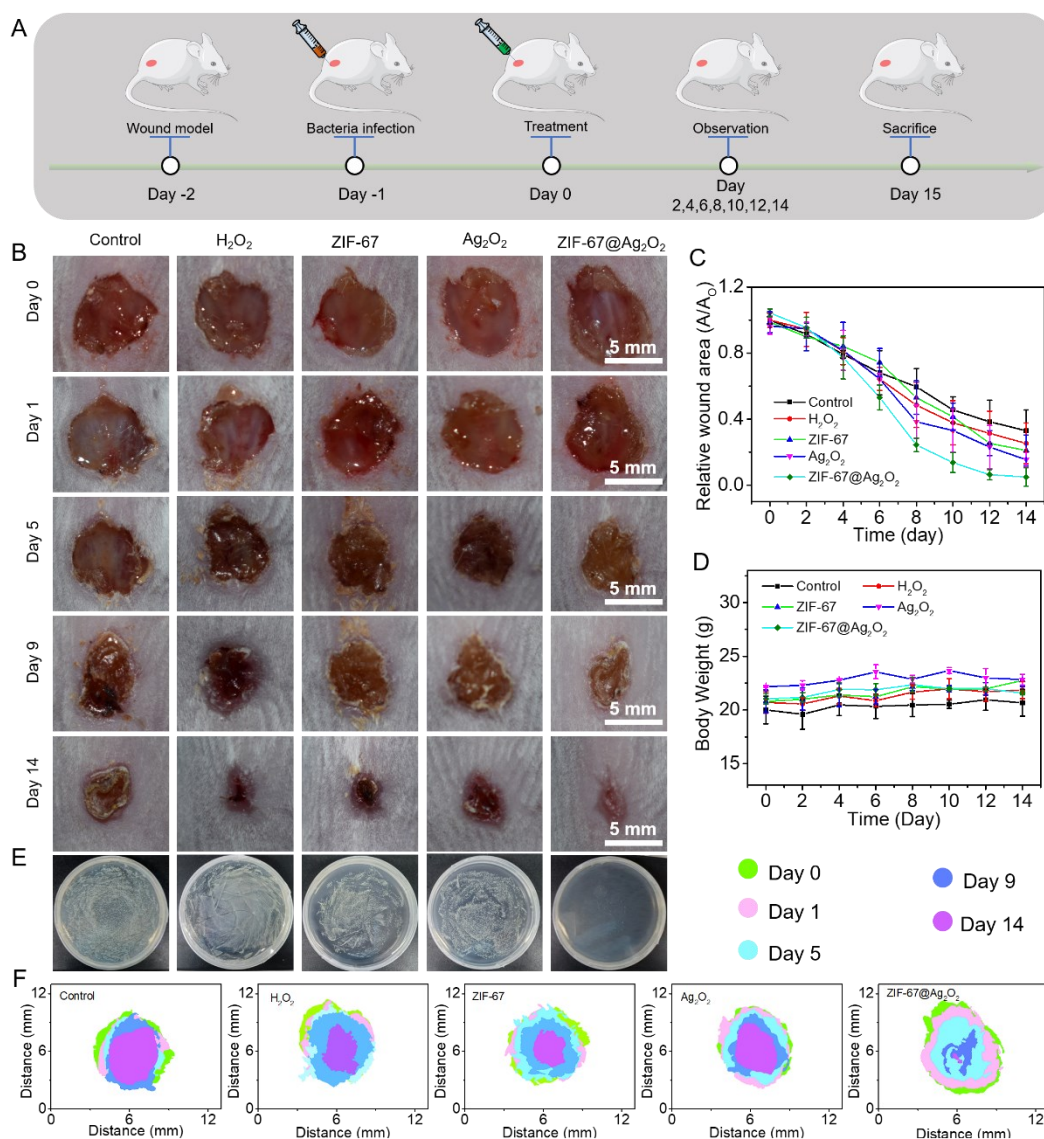


**Figure 7.** (A) Schematic illustration of antibacterial protocol *in vivo*. (B) Representative wound photographic images of mice after various treatments at different times. (C) Relative area changes of *S. aureus*-infected wounds during treatment. (D) Body weight measurements of mice infected by *S. aureus* during treatment. (E) Photographic images of bacterial colonies of *S. aureus* obtained from infected wound tissues. (F) Traces of wound closure in mice of different groups. The data are shown as a mean ± SD (n = 3).

To more intuitively reflected the effect of wound healing, typical pathological sections of each group were obtained after the various treatments and prepared by H&E staining, and Masson staining at the 14th day. As shown in Figure 8A, incomplete skin structures without an epidermal layer were observed after therapy, indicating that the *S. aureus*-infected wound did not healed after 14 days of treatment with PBS buffer, $H_2O_2$, ZIF-67 nanosheets or $Ag_2O_2$ NPs. In contrast, after being treated with ZIF-67@$Ag_2O_2$ nanosheets, the epidermis gradually formed and there was more collagenous fiber regeneration in the dermis layer (blue in Masson staining) in keratinized layer. The inflammatory response is an important signal of bacterial infection, so immunohistochemical staining was also used to evaluate the degree of angiogenesis in the skin. Cluster of differentiation 31 (CD31) is a well-recognized marker for endothelial cells and can be used as an indicator of angiogenesis. As shown in Figure 8B, there was more intensive staining of CD31 in the ZIF-67@$Ag_2O_2$ nanosheets group, suggesting that ZIF-67@$Ag_2O_2$ nanosheets effectively resisted *S. aureus* infection and promoted cell proliferation. Overall, our findings demonstrate that the designed ZIF-67@$Ag_2O_2$ nanosheets exhibit excellent wound-healing performance and biocompatibility *in vivo*.
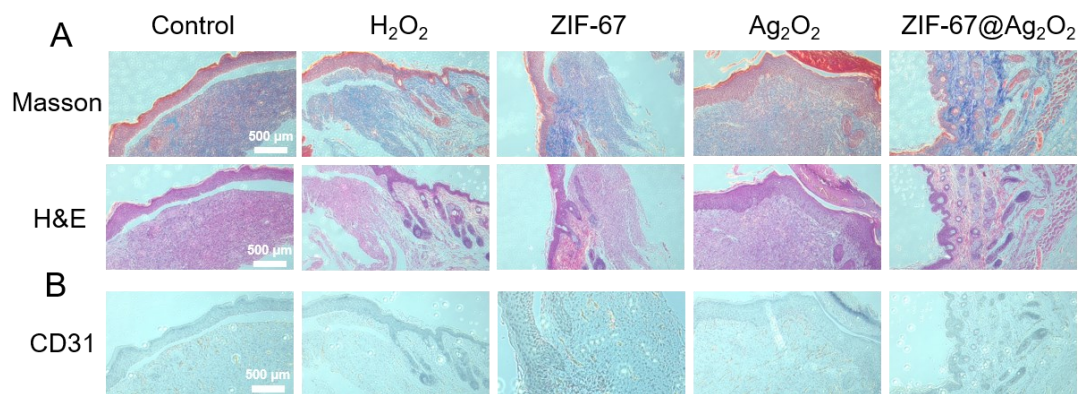
**Figure 8.** (A) Histological photomicrographs of skin tissue sections by H&E staining, Masson staining and (B) immunohistochemistry CD31 staining on day 14 after different treatments.

Finally, to evaluate the *in vivo* toxicity of the ZIF-67@Ag$_2$O$_2$ nanosheets, the bodyweight of the mice was monitored in addition to the mass of several main organs after treatment with the ZIF-67@Ag$_2$O$_2$ nanosheets. As Figure 7D indicates, the weight results showed no significant variation during the treatment period. Additionally, as shown in Figure 9, the main organs of the treated mice did not show signs of damage or pathological change. Furthermore, to evaluated the biological safety of ZIF-67@Ag$_2$O$_2$ nanosheets, the expression levels of typical pro-inflammatory cytokines in the serum of infected mice after different treatment were assessed by ELISA. As shown in Figure S14, compared with PBS (control), H$_2$O$_2$, ZIF-67 and Ag$_2$O$_2$ groups illustrated a slight decrease in the level of IL-6 and IL-1β, due to the limited therapeutic efficiency. In contrast, the ZIF-67@Ag$_2$O$_2$ nanosheets group presented no significant difference to the normal group, which demonstrated the *in vivo* anti-inflammatory ability of ZIF-67@Ag$_2$O$_2$ nanosheets. Similar levels of TNF-α expression were found

between the control and other groups, as the ZIF-67@Ag$_2$O$_2$ nanosheets group alone

did not exhibited significantly activation of immunoreactivity. Once again, these results

showed that the ZIF-67@Ag$_2$O$_2$ nanosheets had no observable biological toxicity *in*

*vivo*.
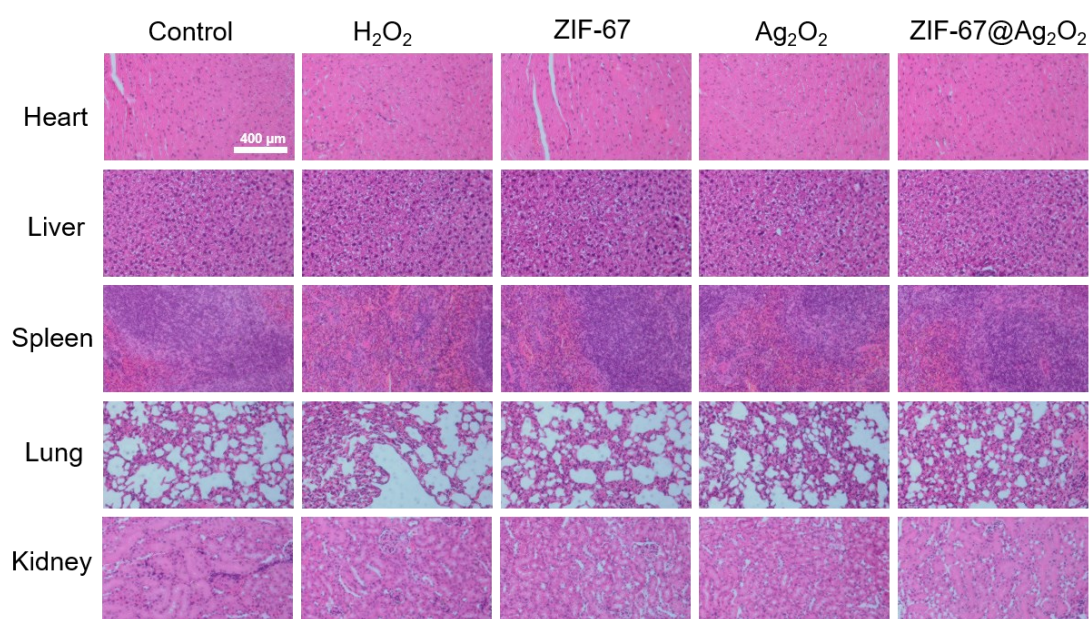


**Figure 9.** H&E staining images of major mice organs on day 14 after different

treatments.

# 4 CONCLUSIONS

In summary, a pH-responsive, multi-functional ZIF-67@Ag$_2$O$_2$ nanoplatform with

H$_2$O$_2$ self-generation ability and enhanced CDT synergistic antibacterial infection

performance was successfully designed and constructed for the first time. The

nanoplatform was synthesized by *in situ* growth of Ag$_2$O$_2$ NPs on the surface of

ultrathin ZIF-67 nanosheets. We confirmed that under the IME mildly acidic conditions,

the pH-responsive behavior of ZIF-67@Ag$_2$O$_2$ nanosheets allowed the simultaneous

generation of H$_2$O$_2$ and Co$^{2+}$ ions by degradation pathways. The elevated H$_2$O$_2$ was

effectively transformed into more harmful •OH by a Fenton-like reaction. The significantly enhanced generation of super-active •OH induced intracellular oxidative stress for reinforced CDT. Both *in vitro* and *in vivo* tests confirmed that ZIF-67@Ag$_2$O$_2$ nanosheets possessed superior antibacterial properties, exhibited favorable biocompatibility, and accelerated the healing of infected wounds. Taken together, our work demonstrates a promising activatable antibacterial alternative for IME-triggered chemodynamic antibacterial therapy. Additionally, the results offer new insight to guide exploration of other IME-activated nanoplatforms for the development of specific safer anti-bacterial therapeutic materials.

**ASSOCIATED CONTENT**

**Supporting Information**

Characterization of the ZIF-67@Ag$_2$O$_2$ nanosheets; AFM images of ZIF-67 nanosheets alongside the corresponding height profile (Figure S1). XRD patterns of ZIF-67 nanosheets (Figure S2). TGA profile of ZIF-67 nanosheets (Figure S3). TEM images of ZIF-67@Ag$_2$O$_2$ (Figure S4). Energy-dispersive X-ray spectrum (EDS) of ZIF-67@Ag$_2$O$_2$ nanosheets (Figure S5). Elemental mapping of ZIF-67 nanosheets (Figure S6). (A) XPS spectra of Ag 3d and (B) Co 2p ZIF-67@Ag$_2$O$_2$ nanosheets (Figure S7). Surface $\zeta$ potentials of each formulation (Figure S8). Cumulative Ag$^+$ release from ZIF-67@Ag$_2$O$_2$ nanosheets at pH 7.4 and pH 6.0, showing their acid-induced dissociation (Figure S9). TEM images of ZIF-67@Ag$_2$O$_2$ at pH 7.4 and 6.0 at different time points (Figure S10). Photographs of bacterial colonies and relative bacterial survival after

treatment with different weight ratios of ZIF-67/$Ag_2O_2$ (pH 7.4 and 6.0) (Figure S11). Histological photomicrographs of skin tissue sections by H&E staining, on day 2 and 4 after different treatments (Figure S12). Giemsa staining images on day 2, and 4 after different treatments (marked by red arrows) (Figure S13). IL-1 β, IL-6 and TNF-α levels of infected mice serum tested by ELISA on day 14 (Figure S14).

## Author Contributions

M.X.: conceptualization, biology experiments, data curation, formal analysis, investigation, visualization, methodology, and writing-original draft preparation. F.T.: resources, visualization. W.L.: visualization. Y. J.: formal analysis. Y.D.: animal care. P.D.T.: validation, writing, review and editing. L.W.: conceptualization, supervision, and funding acquisition. Q.Y: conceptualization, funding acquisition, and project administration.

**Notes**

The authors declare no competing financial interest.

**AUTHOR INFORMATION**

**Corresponding Authors**

LinGe Wang − South China Advanced Institute for Soft Matter Science and Technology, School of Emergent Soft Matter, Guangdong Provincial Key Laboratory of Functional and Intelligent Hybrid Materials and Devices, South China University of Technology, Guangzhou 510640, P. R. China;

orcid.org/0000-0002-5534-5466; Email: lingewang@scut.edu.cn

Qianqian Yu − South China Advanced Institute for Soft Matter Science and Technology, School of Emergent Soft Matter, Guangdong Provincial Key Laboratory of Functional and Intelligent Hybrid Materials and Devices, South China University of Technology, Guangzhou 510640, P. R. China;

orcid.org/0000-0001-5731-3356; Email: yuqianqian@scut.edu.cn

**Authors**

Mengmeng Xu- South China Advanced Institute for Soft Matter Science and Technology, School of Emergent Soft Matter, Guangdong Provincial Key Laboratory of Functional and Intelligent Hybrid Materials and Devices, South China University of Technology, Guangzhou 510640, P. R. China;

Fangrong Tan- South China Advanced Institute for Soft Matter Science and Technology, School of Emergent Soft Matter, Guangdong Provincial Key Laboratory of Functional and Intelligent Hybrid Materials and Devices, South China University of Technology, Guangzhou 510640, P. R. China;

Wanru Luo- South China Advanced Institute for Soft Matter Science and Technology, School of Emergent Soft Matter, Guangdong Provincial Key Laboratory of Functional and Intelligent Hybrid Materials and Devices, South China University of Technology, Guangzhou 510640, P. R. China;

Yifan Jia- South China Advanced Institute for Soft Matter Science and Technology, School of Emergent Soft Matter, Guangdong Provincial Key Laboratory of Functional and Intelligent Hybrid Materials and Devices, South China University of Technology, Guangzhou 510640, P. R. China;

Yan Deng- South China Advanced Institute for Soft Matter Science and Technology, School of Emergent Soft Matter, Guangdong Provincial Key Laboratory of Functional and Intelligent Hybrid Materials and Devices, South China University of Technology, Guangzhou 510640, P. R. China;

Paul D. Topham- Chemical Engineering and Applied Chemistry, School of Infrastructure and Sustainable Engineering, College of Engineering and Physical Sciences, Aston University, Birmingham, B4 7ET, UK.

**REFERENCES**

(1) Zhang, Z.; Xie, J.; Xing, J.; Li, C.; Wong, T. M.; Yu, H.; Li, Y.; Yang, F.; Tian, Y.; Zhang, H.; et al. Light-Programmable Nanocomposite Hydrogel for State-Switchable Wound Healing Promotion and Bacterial Infection Elimination Adv Healthc Mater 2023, 12, e2201565.

(2) Xie, W.; Chen, J.; Cheng, X.; Feng, H.; Zhang, X.; Zhu, Z.; Dong, S.; Wan, Q.; Pei, X.; Wang, J. Multi-Mechanism Antibacterial Strategies Enabled by Synergistic Activity of Metal-Organic Framework-Based Nanosystem for Infected Tissue Regeneration Small 2023, e2205941.

(3) Ge, C.; Wu, R.; Chong, Y.; Fang, G.; Jiang, X.; Pan, Y.; Chen, C.; Yin, J.-J. Synthesis of Pt Hollow Nanodendrites with Enhanced Peroxidase-Like Activity against Bacterial Infections: Implication for Wound Healing Adv. Funct. Mater. 2018, 28, 1801484.

(4) Gnanasekar, S.; Kasi, G.; He, X.; Zhang, K.; Xu, L.; Kang, E. T. Recent Advances in Engineered Polymeric Materials for Efficient Photodynamic Inactivation of Bacterial Pathogens Bioact Mater 2023, 21, 157-174.

(5) Gupta, A.; Das, R.; Yesilbag Tonga, G.; Mizuhara, T.; Rotello, V. M. Charge-Switchable Nanozymes for Bioorthogonal Imaging of Biofilm-Associated Infections ACS Nano 2018, 12, 89-94.

(6) Yu, Q.; Deng, T.; Lin, F. C.; Zhang, B.; Zink, J. I. Supramolecular Assemblies of

Heterogeneous Mesoporous Silica Nanoparticles to Co-deliver Antimicrobial Peptides and Antibiotics for Synergistic Eradication of Pathogenic Biofilms ACS Nano 2020, 14, 5926-5937.

(7) Yuan, Z.; Lin, C.; He, Y.; Tao, B.; Chen, M.; Zhang, J.; Liu, P.; Cai, K. Near-Infrared Light-Triggered Nitric-OxideEnhanced Photodynamic Therapy and LowTemperature Photothermal Therapy for Biofilm Elimination ACS Nano 2020, 14, 3546-3562.

(8) Cai, X.; Jiao, L.; Yan, H.; Wu, Y.; Gu, W.; Du, D.; Lin, Y.; Zhu, C. Nanozyme-Involved Biomimetic Cascade Catalysis for Biomedical Applications Mater. Today 2021, 44, 211-228.

(9) Yang, B.; Chen, Y.; Shi, J. Reactive Oxygen Species (ROS)-Based Nanomedicine Chem. Rev. 2019, 119, 4881-4985.

(10) Jia, C.; Guo, Y.; Wu, F. G. Chemodynamic Therapy via Fenton and Fenton-Like Nanomaterials: Strategies and Recent Advances Small 2022, 18, e2103868.

(11) Lai, L.; Zou, W.; Zhang, Y.; Tu, Y.; Li, S.; Xin, T.; Zhou, T.; Xu, S.; Zheng, P.; Pan, Q.; et al. Multifunctional MIL-101 Nanoparticles with Fenton-like Reactions to Co-Deliver LL-37 Peptide and Vancomycin for Targeted NIR Imaging and Drug-Resistant Bacteria Treatment Chem. Eng. J. 2022, 435, 135084.

(12) Peng, L.; Yang, X.; Wang, S.; Chan, Y. K.; Chen, Y.; Yang, Z.; Mao, Y.; Li, L.; Yang, W.; Deng, Y. Bimetal Metal–Organic Framework Domino Microreactor for Synergistic Antibacterial Starvation/Chemodynamic Therapy and Robust Wound Healing Nanoscale 2022, 14, 2052-2064.

(13) Zhou, X.; Wang, Z.; Chan, Y. K.; Yang, Y.; Jiao, Z.; Li, L.; Li, J.; Liang, K.; Deng,

Y. Infection Micromilieu-Activated Nanocatalytic Membrane for Orchestrating Rapid Sterilization and Stalled Chronic Wound Regeneration Adv. Fun. Mater. 2021, 32, 2109469.

(14) Wang, T.; Dong, D.; Chen, T.; Zhu, J.; Wang, S.; Wen, W.; Zhang, X.; Tang, H.; Liang, J.; Wang, S.; et al. Acidity-Responsive Cascade Nanoreactor Based on Metal-Nanozyme and Glucose Oxidase Combination for Starving and Photothermal-Enhanced Chemodynamic Antibacterial Therapy Chem. Eng. J. 2022, 446, 137172.

(15) Chen, H.; Cheng, J.; Cai, X.; Han, J.; Chen, X.; You, L.; Xiong, C.; Wang, S. pH-Switchable Antimicrobial Supramolecular Hydrogels for Synergistically Eliminating Biofilm and Promoting Wound Healing ACS Appl. Mater. Interfaces 2022, 14, 18120-18132.

(16) Lin, L.; Gong, H.; Li, R.; Huang, J.; Cai, M.; Lan, T.; Huang, W.; Guo, Y.; Zhou, Z.; An, Y.; et al. Nanodrug with ROS and pH Dual-Sensitivity Ameliorates Liver Fibrosis via Multicellular Regulation Adv. Sci. 2020, 7, 1903138.

(17) Zhang, Y.; Lai, L.; Liu, Y.; Chen, B.; Yao, J.; Zheng, P.; Pan, Q.; Zhu, W. Biomineralized Cascade Enzyme-Encapsulated ZIF-8 Nanoparticles Combined with Antisense Oligonucleotides for Drug-Resistant Bacteria Treatment ACS Appl. Mater. Interfaces 2022, 14, 6453-6464.

(18) Bergs, C.; Brück, L.; Rosencrantz, R. R.; Conrads, G.; Elling, L.; Pich, A. Biofunctionalized Zinc Peroxide ($ZnO_2$) Nanoparticles as Active Oxygen Sources and Antibacterial Agents RSC Advances 2017, 7, 38998-39010.

(19) Zhao, Y.; Zhu, Y.; Yang, G.; Xia, L.; Yu, F.; Chen, C.; Zhang, L.; Cao, H. A

pH/H$_2$O$_2$ Dual Triggered Nanoplatform for Enhanced Photodynamic Antibacterial Efficiency J. Mater. Chem. B 2021, 9, 5076-5082.

(20) Han, Y.; Ouyang, J.; Li, Y.; Wang, F.; Jiang, J. H. Engineering H$_2$O$_2$ Self-Supplying Nanotheranostic Platform for Targeted and Imaging-Guided Chemodynamic Therapy ACS Appl. Mater. Interfaces 2020, 12, 288-297.

(21) Wu, D.; Zhu, Z.-Q.; Tang, H.-X.; Shi, Z.-E.; Kang, J.; Liu, Q.; Qi, J. Efficacy-shaping Nanomedicine by Loading Calcium Peroxide into Tumor Microenvironment-responsive Nanoparticles for the Antitumor Therapy of Prostate Cancer Theranostics 2020, 10, 9808-9829.

(22) Zhang, M.; Song, R.; Liu, Y.; Yi, Z.; Meng, X.; Zhang, J.; Tang, Z.; Yao, Z.; Liu, Y.; Liu, X.; et al. Calcium-Overload-Mediated Tumor Therapy by Calcium Peroxide Nanoparticles Chem 2019, 5, 2171-2182.

(23) Lin, L. S.; Wang, J. F.; Song, J.; Liu, Y.; Zhu, G.; Dai, Y.; Shen, Z.; Tian, R.; Song, J.; Wang, Z.; et al. Cooperation of Endogenous and Exogenous Reactive Oxygen Species Induced by Zinc Peroxide Nanoparticles to Enhance Oxidative Stress-Based Cancer Therapy Theranostics 2019, 9, 7200-7209.

(24) Zhang, D.; Chen L.; Xu M. M.; Feng G. j.; Zhang B. X.; Zhang H.; Yang C. Y.; Yu Q. Q.; Wang L. G.Visible-Light Responsive PVDF/Carbon Sphere@TiO$_2$ Membrane for Dye Scavenging and Bacteria Inactivation Appl. Surf. Sci. 2022. 605 154755.

(25) Gao, S.; Jin, Y.; Ge, K.; Li, Z.; Liu, H.; Dai, X.; Zhang, Y.; Chen, S.; Liang, X.; Zhang, J. Self-Supply of O$_2$ and H$_2$O$_2$ by a Nanocatalytic Medicine to Enhance Combined Chemo/Chemodynamic Therapy Adv. Sci. 2019, 6, 1902137.

(26) Li, X.; Liang, M.; Jiang, S.; Cao, S.; Li, S.; Gao, Y.; Liu, J.; Bai, Q.; Sui, N.; Zhu, Z. Pomegranate-Like $CuO_2@SiO_2$ Nanospheres as $H_2O_2$ Self-Supplying and Robust Oxygen Generators for Enhanced Antibacterial Activity ACS Appl. Mater. Interfaces 2021, 13, 22169-22181.

(27) Tang, Z. M.; Liu, Y. Y.; Ni, D. L.; Zhou, J. J.; Zhang, M.; Zhao, P. R.; Lv, B.; Wang, H.; Jin, D. Y.; Bu, W. B. Biodegradable Nanoprodrugs: "Delivering" ROS to Cancer Cells for Molecular Dynamic Therapy Adv. Mater. 2020, 32, e1904011.

(28) Lin, L. S.; Huang, T.; Song, J.; Ou, X. Y.; Wang, Z.; Deng, H.; Tian, R.; Liu, Y.; Wang, J. F.; Liu, Y.; et al. Synthesis of Copper Peroxide Nanodots for $H_2O_2$ Self-Supplying Chemodynamic Therapy J. Am. Chem. Soc. 2019, 141, 9937-9945.

(29) Li, M.; Lan, X.; Han, X.; Shi, S.; Sun, H.; Kang, Y.; Dan, J.; Sun, J.; Zhang, W.; Wang, J. Acid-Induced Self-Catalyzing Platform Based on Dextran-Coated Copper Peroxide Nanoaggregates for Biofilm Treatment ACS Appl. Mater. Interfaces 2021, 13, 29269-29280.

(30) Liu, L.; Wang, C.; Li, Y.; Qiu, L.; Zhou, S.; Cui, P.; Jiang, P.; Ni, X.; Liu, R.; Du, X.; et al. Manganese Dioxide Nanozyme for Reactive Oxygen Therapy of Bacterial Infection and Wound Healing Biomater. Sci. 2021, 9, 5965-5976.

(31) Liu, Y.; Nie, N.; Tang, H.; Zhang, C.; Chen, K.; Wang, W.; Liu, J. Effective Antibacterial Activity of Degradable Copper-Doped Phosphate-Based Glass Nanozymes ACS Appl. Mater. Interfaces 2021, 13, 11631-11645.

(32) Fang, Y.; Wang, H. M.; Gu, Y. X.; Yu, L.; Wang, A. J.; Yuan, P. X.; Feng, J. J. Highly Enhanced Electrochemiluminescence Luminophore Generated by Zeolitic

Imidazole Framework-8-Linked Porphyrin and Its Application for Thrombin Detection Anal. Chem. 2020, 92, 3206-3212.

(33) Liu, X.; Yan, Z.; Zhang, Y.; Liu, Z.; Sun, Y.; Ren, J.; Qu, X. Two-Dimensional Metal−Organic Framework/ Enzyme Hybrid Nanocatalyst as a Benign and Self-Activated Cascade Reagent for in Vivo Wound Healing ACS Nano 2019, 13, 5222-5230.

(34) Zhang, W.; Zhou, Y.; Fan, Y.; Cao, R.; Xu, Y.; Weng, Z.; Ye, J.; He, C.; Zhu, Y.; Wang, X. Metal–Organic-Framework-Based Hydrogen-Release Platform for Multieffective Helicobacter Pylori Targeting Therapy and Intestinal Flora Protective Capabilities Adv. Mater. 2021, 34, e2105738.

(35) Huang, Y.; Geng, H.; Wu, Z.; Sun, L.; Ji, C.; Grimes, C. A.; Feng, X.; Cai, Q. An $Ag_2S$@ZIF-Van Nanosystem for NIR-II Imaging of Bacterial-induced Inflammation and Treatment of Wound Bacterial Infection Biomater. Sci. 2022, 10, 3972-3980.

(36) Wang, Z.; Zhou, X.; Li, Y.; Huang, Z.; Han, J.; Xie, G.; Liu, J. Sensing ATP: Zeolitic Imidazolate Framework-67 Is Superior to Aptamers for Target Recognition Anal. Chem. 2021, 93, 7707-7713.

(37) Aguado, S.; Quiros, J.; Canivet, J.; Farrusseng, D.; Boltes, K.; Rosal, R. Antimicrobial Activity of Cobalt Imidazolate Metal–Organic Frameworks Chemosphere 2014, 113, 188-192.

(38) Fan, X.; Wu, X.; Yang, F.; Wang, L.; Ludwig, K.; Ma, L.; Trampuz, A.; Cheng, C.; Haag, R. A Nanohook-Equipped Bionanocatalyst for Localized Near-InfraredEnhanced Catalytic Bacterial Disinfection Angew. Chem. Int. Ed. 2022, 61, e202113833.

(39) Qian, L.; Lei, D.; Duan, X.; Zhang, S.; Song, W.; Hou, C.; Tang, R. Design and

Preparation of Metal-Organic Framework Papers with Enhanced Mechanical Properties and Good Antibacterial Capacity Carbohydr. Polym. 2018, 192, 44-51.

(40) Wu, J.; Shen, P.; Qin, X.; Yang, Y.; Lin, C.; Li, X.; Geng, W.; Gao, P.; Chen, L.; Miao, L.; et al. Self-supply of $H_2O_2$ and $O_2$ by a Composite Nanogenerator for Chemodynamic Therapy/hypoxia Improvement and Rapid Therapy of Biofilm-Infected Wounds Chem. Eng. J. 2023, 459, 141507.

(41) Chen, J.; Bao, X.; Meng, T.; Sun, J.; Yang, X. Zeolitic Imidazolate Framework-67 Accelerates Infected Diabetic Chronic Wound Healing Chem. Eng. J. 2022, 430, 133091.

(42) Huang, Y.; Zhao, M.; Han, S.; Lai, Z.; Yang, J.; Tan, C.; Ma, Q.; Lu, Q.; Chen, J.; Zhang, X.; et al. Growth of Au Nanoparticles on 2D Metalloporphyrinic Metal-Organic Framework Nanosheets Used as Biomimetic Catalysts for Cascade Reactions Adv. Mater. 2017, 29, 1700102.

(43) Hu, W. C.; Younis, M. R.; Zhou, Y.; Wang, C.; Xia, X. H. In Situ Fabrication of Ultrasmall Gold Nanoparticles/2D MOFs Hybrid as Nanozyme for Antibacterial Therapy Small 2020, 16, e2000553.

(44) He, C.; Lu, K.; Liu, D.; Lin, W. Nanoscale Metal−Organic Frameworks for the Co-Delivery of Cisplatin and Pooled siRNAs to Enhance Therapeutic Efficacy in Drug-Resistant Ovarian Cancer Cells J. Am. Chem. Soc. 2014, 136, 5181-5184.

(45) Sun, D.; Yang, D.; Wei, P.; Liu, B.; Chen, Z.; Zhang, L.; Lu, J. One-Step Electrodeposition of Silver Nanostructures on 2D/3D Metal−Organic Framework ZIF-67: Comparison and Application in Electrochemical Detection of Hydrogen Peroxide

ACS Appl. Mater. Interfaces 2020, 12, 41960-41968.

(46) Gao, X.; Wei, M.; Ma, D.; Yang, X.; Zhang, Y.; Zhou, X.; Li, L.; Deng, Y.; Yang, W. Engineering of a Hollow-Structured $Cu_{2-x}S$ NanoHomojunction Platform for Near Infrared-Triggered Infected Wound Healing and Cancer Therapy Adv. Funct. Mater. 2021, 31, 2106700.

(47) Ma, Y.; Jiang, K.; Chen, H.; Shi, Q.; Liu, H.; Zhong, X.; Qian, H.; Chen, X.; Cheng, L.; Wang, X. Liquid Exfoliation of $V_8C_7$ Nanodots as Peroxidase-like Nanozymes for Photothermal-Catalytic Synergistic Antibacterial Treatment Acta Biomater. 2022, 149, 359-372.

(48) Qi, Y.; Ren, S.; Ye, J.; Tian, Y.; Wang, G.; Zhang, S.; Du, L.; Li, Y.; Che, Y.; Ning, G. Infection Microenvironment-Activated Core-Shell Nanoassemblies for Photothermal/Chemodynamic Synergistic Wound Therapy and Multimodal Imaging Acta Biomater. 2022, 143, 445-458.

(49) Zhou, H.; Zheng, M.; Tang, H.; Xu, B.; Tang, Y.; Pang, H. Amorphous Intermediate Derivative from ZIF-67 and Its Outstanding Electrocatalytic Activity Small 2020, 16, e1904252.

(50) Bi, X.; Bai, Q.; Liang, M.; Yang, D.; Li, S.; Wang, L.; Liu, J.; Yu, W. W.; Sui, N.; Zhu, Z. Silver Peroxide Nanoparticles for Combined Antibacterial Sonodynamic and Photothermal Therapy Small 2021, 18, e2104160.

Table Of Contents (TOC) graphic：

Treat

Two weeks

**Acidic Microenvironment**

Live Bacteria

$Ag_2O_2 + 2H^+ \longrightarrow H_2O_2 + 2Ag^+$

$H_2O_2$ self-sufficient

$H_2O_2 \xrightarrow{Co^{2+}} \cdot OH$

Chemodynamic Therapy

DNA damage

Cell wall rupture

Recovery

ZIF-67@Ag$_2$O$_2$

Acid Degradation

$ZIF\text{-}67 \xrightarrow{H^+} Co^{2+}$

Dead Bacteria